A cross-correlation study between the cosmological 21 cm signal and the kinetic Sunyaev-Zel'dovich effect

Jelić, Vibor; Zaroubi, Saleem; Aghanim, Nabila; Douspis, Marian; Koopmans, Léon V. E.; Langer, Mathieu; Mellema, Garrelt; Tashiro, Hiroyuki; Thomas, Rajat M.

Published in:
Monthly Notices of the Royal Astronomical Society

DOI:
10.1111/j.1365-2966.2009.16086.x

Monthly Notices
of the
ROYAL ASTRONOMICAL SOCIETY

Mon. Not. R. Astron. Soc. **402,** 2279–2290 (2010) doi:10.1111/j.1365-2966.2009.16086.x

A cross-correlation study between the cosmological 21 cm signal and the kinetic Sunyaev–Zel'dovich effect

Vibor Jelić,[1⋆] Saleem Zaroubi,[1] Nabila Aghanim,[2,3] Marian Douspis,[2,3] Léon V. E. Koopmans,[1] Mathieu Langer,[2,3] Garrelt Mellema,[4] Hiroyuki Tashiro[2,3] and Rajat M. Thomas[1,5]

[1] *Kapteyn Astronomical Institute, University of Groningen, PO Box 800, 9700 AV Groningen, the Netherlands*
[2] *Institut d'Astrophysique Spatiale (IAS), Bâtiment 121, F-91405, Orsay, France*
[3] *Université Paris-Sud XI and CNRS (UMR 8617), France*
[4] *Stockholm Observatory, AlbaNova University Center, Stockholm University, SE-106 91, Stockholm, Sweden*
[5] *Institute for the Mathematics and Physics of the Universe (IPMU), The University of Tokyo, Chiba 277-8582, Japan*

Accepted 2009 November 18. Received 2009 November 17; in original form 2009 July 19

ABSTRACT

The Universe's Epoch of Reionization can be studied using a number of observational probes that provide complementary or corroborating information. Each of these probes suffers from its own systematic and statistical uncertainties. It is therefore useful to consider the mutual information that these data sets contain. In this paper, we present a cross-correlation study between the kinetic Sunyaev–Zel'dovich effect – produced by the scattering of cosmic microwave background (CMB) photons off free electrons produced during the reionization process – and the cosmological 21 cm signal – which reflects the neutral hydrogen content of the Universe, as a function of redshift. The study is carried out using a simulated reionization history in $100\,h^{-1}$ Mpc scale N-body simulations with radiative transfer. In essence, we find that the two probes anticorrelate. The significance of the anticorrelation signal depends on the extent of the reionization process, wherein extended histories result in a much stronger signal compared to instantaneous cases. Unfortunately, however, once the primary CMB fluctuations are included into our simulation they serve as a source of large correlated noise that renders the cross-correlation signal insignificant, regardless of the reionization scenario.

Key words: cosmic microwave background – cosmology: theory – diffuse radiation – large-scale structure of Universe – radio lines: general.

1 INTRODUCTION

The Epoch of Reionization (EoR) is one of the least explored periods in the history of the Universe. At present, there are only a few tentative observational constraints on the EoR such as the Gunn–Peterson troughs (Gunn & Peterson 1965; Fan et al. 2006) and the cosmic microwave background (CMB) E-mode polarization (Page et al. 2007) at large scales. Both of these observations provide strong yet limited constraints on the EoR. In the near future, however, a number of observations at various wavelengths [e.g. redshifted 21 cm from H I, Lyman α emitters, high redshift quasi-stellar objects (QSOs) etc.] are expected to probe this pivotal epoch in much greater detail. Among these, the cosmological 21 cm transition line of neutral hydrogen is the most promising probe of the intergalactic medium during reionization (Madau, Meiksin & Rees 1997)

A number of radio telescopes [e.g. Low Frequency Array (LOFAR),[1] Murchison Widefield Array (MWA)[2] and Square Kilometre Array (SKA)[3]] are currently being constructed/designed that aim at detecting the redshifted 21 cm line to study the EoR. Unfortunately, these experiments will suffer from a high degree of contamination, due to both astrophysical interlopers such as the Galactic and extragalactic foregrounds, and non-astrophysical instrumental effects (e.g. Jelić et al. 2008; Labropoulos et al. 2009). Fortunately, the signal has some characteristics which differentiate it from the foregrounds and noise, and using proper statistics makes it possible to extract signatures of reionization (e.g. Furlanetto, Zaldarriaga & Hernquist 2004; Harker et al. 2009a,b). In order to reliably detect the cosmological signal from the observed

⋆E-mail: vjelic@astro.rug.nl

[1] http://www.lofar.org
[2] http://www.haystack.mit.edu/ast/arrays/mwa
[3] http://www.skatelescope.org

data, it is essential to understand in detail all aspects of the data and their influence on the extracted signal.

Given the challenges and uncertainties involved in measuring the redshifted 21 cm signal from the EoR, it is vital to corroborate this result with other probes of the EoR. In this paper, we study the information imprinted on the CMB by the EoR and its cross-correlation with the 21 cm probe. Given the recent launch of the *Planck* satellite, which will measure the CMB with unprecedented accuracy, it is fit to conduct a rigorous study into the cross-correlation of these data sets.

One of the leading sources of secondary anisotropies in the CMB is due to the scattering of CMB photons off free electrons, created during the reionization process (Zeldovich & Sunyaev 1969). The effect of anisotropies when induced by thermal motions of free electrons is called the thermal Sunyaev–Zel'dovich effect (tSZ) and when due to bulk motion of free electrons, the kinetic Sunyaev–Zel'dovich effect (kSZ). The latter is far more dominant during reionization (for a review of secondary CMB effects, see e.g. Aghanim, Majumdar & Silk 2008).

The kSZ effect from a homogeneously ionized medium, i.e. with ionized fraction only a function of redshift, has been studied both analytically and numerically by a number of authors; the linear regime of this effect was first calculated by Sunyaev & Zeldovich (1970) and subsequently revisited by Ostriker & Vishniac (1986) and Vishniac (1987) – hence also referred to as the Ostriker–Vishniac (OV) effect. In recent years, various groups have calculated this effect in its non-linear regime using semi-analytical models and numerical simulations (Gnedin & Jaffe 2001; Santos et al. 2003; Zhang, Pen & Trac 2004). These studies show the contribution due to non-linear effects being important only at small angular scales ($l > 1000$), while the OV effect dominates at large angular scales.

The kSZ effect from patchy reionization was first estimated using simplified semi-analytical models (Santos et al. 2003) wherein they concluded that fluctuations caused by patchy reionization dominate over anisotropies induced by homogeneous reionization. However, for a complete picture of the CMB anisotropies induced by the EoR, a more detailed modelling is required. Over and above the underlying density and velocity fields, these details should include the formation history and 'nature' of the first ionizing sources and the radiative transport of ionizing photons to derive the reionization history (sizes and distribution of the ionized bubbles). Some recent numerical simulations of the kSZ effect during the EoR were carried out by Salvaterra et al. (2005), Zahn et al. (2005), Doré et al. (2007) and Iliev et al. (2007).

Cross-correlation between the cosmological 21 cm signal and the secondary CMB anisotropies provide a potentially useful statistic. The cross-correlation has the advantage that the measured statistic is less sensitive to contaminants such as the foregrounds, systematics and noise in comparison to 'auto-correlation' studies. Analytical cross-correlation studies between the CMB temperature anisotropies and the EoR signal on large scales ($l \sim 100$) were carried out by Alvarez et al. (2006), Adshead & Furlanetto (2008) and Lee (2009) and on small scales ($l > 1000$) by Cooray (2004), Salvaterra et al. (2005) and Slosar, Cooray & Silk (2007). Thus far, the only numerical study of the cross-correlation was carried out by Salvaterra et al. (2005). Some additional analytical work on cross-correlation between the E and B modes of CMB polarization with the redshifted 21 cm signal was done by Tashiro et al. (2008) and Dvorkin, Hu & Smith (2009).

In this paper, we first calculate the kSZ anisotropies from homogeneous and patchy reionization based on $100\,h^{-1}$ Mpc scale numerical simulations of reionization. We then cross-correlate them with the expected EoR maps obtained from the same simulations, and we discuss how the large-scale velocities and primary CMB (pCMB) fluctuations influence the cross-correlation. Although similar in some aspects, the work presented here differs from Salvaterra et al. (2005) substantially. First, Salvaterra et al. used a relatively small computational box ($20\,h^{-1}$ Mpc) incapable of capturing relevant large-scale density and velocity perturbations. Secondly, the pCMB fluctuations, which manifest themselves as a large background noise, were not taken into account. And finally, there is a difference in the procedure for calculating the cross-correlation coefficient.

The paper is organized as follows. In Section 2, we discuss the kSZ signal and cosmological 21 cm signal from the EoR. In Section 3, we present the numerical simulations employed to obtain the kSZ and EoR maps for a specific reionization history. Cross-correlation between the cosmological 21 cm fluctuations (EoR signal) and the kSZ anisotropies, together with the influence of the large-scale velocities and the pCMB fluctuations on the CMB–EoR cross-correlation, is discussed in Section 4. Finally, in Section 5 we present our discussions and conclusions on the topic.

Throughout we assume Λ cold dark matter (ΛCDM) cosmology with *Wilkinson Microwave Anisotropy Probe* 3 (*WMAP*3) parameters (Spergel et al. 2007): $h = 0.73$, $\Omega_{\rm b} = 0.0418$, $\Omega_{\rm m} = 0.238$ and $\Omega_\Lambda = 0.762$.

2 THEORY

Here we briefly review the theoretical aspects of the kSZ effect and the cosmological 21 cm signal from the EoR. We also present the relevant mathematical forms used to calculate the kSZ and the cosmological 21 cm signals.

2.1 Kinetic Sunayev–Zel'dovich effect

The temperature fluctuation of the CMB caused by the Thompson scattering of its photons off populations of free electrons in bulk motion, for a given line of sight (LOS), is

$$\left(\frac{\delta T}{T}\right)_{\rm kSZ} = -\sigma_{\rm T} \int_{t_{\rm r}}^{t_0} {\rm e}^{-\tau} n_{\rm e} (\hat{\boldsymbol{r}} \cdot \boldsymbol{v}) {\rm d}t, \tag{1}$$

where τ is the optical depth of electrons to the Thomson scattering, $\boldsymbol{v}$ the bulk velocity of free electrons and $\hat{\boldsymbol{r}}$ the unit vector denoting the direction of the LOS. The integral is performed for each LOS with $t_{\rm r}$ being the time at the epoch of recombination and t_0 the age of the Universe today. Note that all quantities are in physical units. Temperature fluctuations produced at time t will be attenuated due to multiple scattering along the LOS to the present time and are accounted for by the ${\rm e}^{-\tau}$ term.

The electron density can be written as the product of the total atom density $n_{\rm n}$ and ionization fraction $x_{\rm e}$. Both $n_{\rm n}$ and $x_{\rm e}$ vary around their average values $\bar{n}_{\rm n}$ and $\bar{x_{\rm e}}$, and thus these fluctuations can be written as $\delta = n_{\rm n}/\bar{n}_{\rm n} - 1$ and $\delta_{x_{\rm e}} = x_{\rm e}/\bar{x}_{\rm e} - 1$, respectively, and consequently the electron density expressed as

$$n_{\rm e} = \bar{n}_{\rm n} \bar{x}_{\rm e} (1 + \delta + \delta_{x_{\rm e}} + \delta\delta_{x_{\rm e}}). \tag{2}$$

In the first approximation, one can just follow the reionization of hydrogen and assume that the atom density equals the hydrogen density. However, in our simulation we follow both hydrogen and helium. Assuming that both hydrogen and helium follow the underlying dark matter density, the atom density is a sum of the total hydrogen ($n_{\rm H}$) and total helium ($n_{\rm He_I}$) densities: $n_{\rm n} = (\bar{n}_{\rm H} + \bar{n}_{\rm He})(1+\delta)$.

Moreover, the electron density can be written as

$$n_e = n_H x_{H\,II} + n_{He} x_{He\,II} + 2 n_{He} x_{He\,III}, \quad (3)$$

where $x_{H\,II, He\,II, He\,III}$ are ionization fractions of H II, He II and He III, respectively. The ionization fractions are defined as $x_{H\,II} = n_{H\,II}/n_H$, $x_{He\,II} = n_{He\,II}/n_{He}$ and $x_{He\,III} = n_{He\,III}/n_{He}$, respectively.

The mean hydrogen and helium densities vary with redshift as $\bar{n}_{H,He} = \bar{n}_{H(0),He(0)}(1+z)^3$, where $\bar{n}_{H(0),He(0)}$ are the mean hydrogen and helium densities at the present time: $\bar{n}_{H(0)} = 1.9 \times 10^{-7}\,\mathrm{cm}^{-3}$ and $\bar{n}_{He(0)} = 1.5 \times 10^{-8}\,\mathrm{cm}^{-3}$.

By inserting equation (2) into equation (1) and converting equation (1) from an integral in time to one in redshift space[4] (z), we get

$$\left(\frac{\delta T}{T}\right)_{kSZ} = -\sigma_T \bar{n}_{n(0)} \int_{z_r}^{z_0} \frac{(1+z)^2}{H} e^{-\tau} \bar{x}_e \times (1 + \delta + \delta_{x_e} + \delta\delta_{x_e}) v_r \mathrm{d}z, \quad (4)$$

where v_r is the component of $\boldsymbol{v}$ along the LOS ($v_r = \hat{\boldsymbol{r}} \cdot \boldsymbol{v}$) and $\bar{n}_{n(0)} = \bar{n}_{H\,I(0)} + \bar{n}_{He\,I(0)}$. For a ΛCDM universe, the Hubble constant at redshift z is $H = H_0\sqrt{\Omega_m(1+z)^3 + \Omega_\Lambda}$ where H_0 is the present value of the Hubble constant, Ω_m is the matter and Ω_Λ the dark energy density.

For homogeneous reionization histories, i.e. a uniform change in the ionization fraction as a function of redshift, equation (4) becomes

$$\left(\frac{\delta T}{T}\right)_{kSZ} = -\sigma_T \bar{n}_{n(0)} \int_{z_r}^{z_0} \frac{(1+z)^2}{H} e^{-\tau} \bar{x}_e (1+\delta) v_r \mathrm{d}z, \quad (5)$$

which means that the kSZ fluctuations are induced only by spatial variations of the density field. The linear regime of this effect is called the OV effect. The OV effect is of second order and peaks at small angular scales (arcminutes) and has an rms of the order of a few μK.

2.2 The cosmological 21 cm signal

In radio astronomy, where the Rayleigh–Jeans law is applicable, the radiation intensity $I(\nu)$ is expressed in terms of the brightness temperature T_b:

$$I(\nu) = \frac{2\nu^2}{c^2} k T_b, \quad (6)$$

where ν is the frequency, c is the speed of light and k is Boltzmann's constant. The predicted differential brightness temperature of the cosmological 21 cm signal with the CMB as the background is given by (Field 1958, 1959; Ciardi & Madau 2003)

$$\delta T_b = 26\,\mathrm{mK}\, x_{H\,I}(1+\delta)\left(1 - \frac{T_{CMB}}{T_s}\right)\left(\frac{\Omega_b h^2}{0.02}\right) \times \left[\left(\frac{1+z}{10}\right)\left(\frac{0.3}{\Omega_m}\right)\right]^{1/2}. \quad (7)$$

Here T_s is the spin temperature, $x_{H\,I}$ is the neutral hydrogen fraction, δ is the matter density contrast and $h = H_0/(100\,\mathrm{km\,s^{-1}\,Mpc^{-1}})$. If we express the neutral hydrogen fraction as $x_{H\,I} = \bar{x}_{H\,I}(1 + \delta_{x_{H\,I}})$, equation (7) becomes

$$\delta T_b = 26\,\mathrm{mK}\, \bar{x}_{H\,I}(1 + \delta + \delta_{x_{H\,I}} + \delta\delta_{x_{H\,I}}) \times \left(1 - \frac{T_{CMB}}{T_s}\right)\left(\frac{\Omega_b h^2}{0.02}\right)\left[\left(\frac{1+z}{10}\right)\left(\frac{0.3}{\Omega_m}\right)\right]^{1/2}. \quad (8)$$

[4] In order to make transformation of equation (1) to the redshift space we use $\mathrm{d}t = -\frac{\mathrm{d}z}{H(z)[1+z]}$, where $H(z)$ is the Hubble constant at redshift z.

In his two seminal papers, Field (1958, 1959) calculated the spin temperature, T_s, as a weighted average of the CMB, kinetic and colour temperatures:

$$T_s = \frac{T_{CMB} + y_{kin} T_{kin} + y_\alpha T_\alpha}{1 + y_{kin} + y_\alpha}, \quad (9)$$

where T_{CMB} is the CMB temperature and y_{kin} and y_α are the kinetic and Lyman α coupling terms, respectively. We assume that the colour temperature, T_α, is equal to T_{kin} (Madau et al. 1997). The kinetic coupling term increases with the kinetic temperature, whereas the y_α coupling term depends on Lyman α pumping through the so-called Wouthuysen–Field effect (Wouthuysen 1952; Field 1958). The two coupling terms are dominant under different conditions and in principle could be used to distinguish between ionization sources, e.g. between first stars, for which Lyman α pumping is dominant, and first mini-quasars for which X-ray photons and therefore heating are dominant (see e.g. Madau et al. 1997; Zaroubi et al. 2007; Thomas & Zaroubi 2008).

3 SIMULATIONS

The kSZ ($\delta T/T$) and the cosmological 21 cm maps (δT_b) are simulated using the following data cubes: density (δ), radial velocity (v_r) and H I, H II, He I, He II and He III fractions ($x_{H\,I, H\,II, He\,I, He\,II\,and\,He\,III}$). The data cubes are produced using the BEARS algorithm, a fast algorithm to simulate the EoR signal (Thomas et al. 2009).

In the following subsections, we summarize the BEARS algorithm and describe the operations preformed on the output in order to calculate the kSZ and the EoR maps. Furthermore, we show in detail the calculations for obtaining the optical depth and the kSZ signal along a certain LOS. Finally, we present the maps of the kSZ temperature fluctuations for the two patchy reionization models ('stars' and 'mini-quasars') and discuss aspects of their contribution to the signal.

3.1 BEARS algorithm: overview

BEARS is a fast algorithm to simulate the underlying cosmological 21 cm signal from the EoR. It is implemented by using an N-body/smoothed particle hydrodynamics (SPH) simulation in conjunction with a 1D radiative transfer code under the assumption of spherical symmetry of the ionized bubbles. The basic steps of the algorithm are as follows. First, a catalogue of 1D ionization profiles of all atomic hydrogen and helium species and the temperature profile that surrounds the source is calculated for different types of ionizing sources with varying masses and luminosities at different redshifts. Subsequently, photon rates emanating from dark matter haloes, identified in the N-body simulation, are calculated semi-analytically. Finally, given the spectrum, luminosity and the density around the source, a spherical ionization bubble is embedded around the source, with a radial profile selected from the catalogue. For more details, we refer to Thomas et al. (2009).

As outputs, we obtain data cubes (2D slices along the frequency/redshift direction) of density (δ), radial velocity (v_r) and hydrogen and helium fractions ($x_{H\,I, H\,II, He\,I, He\,II\,and\,He\,III}$). Each data cube consists of about 850 slices, each representing a certain redshift between 6 and 11.5. This interval is chosen to match the spectral resolution that the frequency-binned LOFAR data will have, i.e. at 0.1 MHz. This implies a δz of about 3×10^{-4} at the lowest redshift ($z = 6$) and ≈0.01 at the high redshift end ($z = 11.5$), which translates to a minimum comoving separation of 0.1 Mpc at low and

<2 Mpc at high redshifts. In both cases, ionized bubbles are sampled extremely well because their typical size (in physical units) is ≈6 Mpc in diameter. Slices have a size of $100\,h^{-1}$ comoving Mpc and are defined on a 512^2 grid. Because these slices are produced to simulate a mock data set for radio-interferometric experiments, they are uniformly spaced in frequency (therefore, not uniform in redshift). Thus, the frequency resolution of the instrument dictates the scales over which structures in the Universe are averaged/smoothed along the redshift direction. The relation between frequency ν and redshift space z is given by

$$z = \frac{\nu_{21}}{\nu} - 1, \tag{10}$$

where $\nu_{21} = 1420$ MHz is the rest frequency that corresponds to the 21 cm line.

The final data cubes are produced using approximately 75 snapshots of the cosmological simulations. Since the choice of the redshift direction in each box is arbitrary, three final data cubes can be produced in this manner (x, y and z).

3.2 Randomization of the structures

The kSZ effect is an integrated effect and is sensitive to the structure distribution along the LOS. To avoid unnatural amplification of the kSZ fluctuations due to repeating structures in the simulated data cubes, we follow the approach of Iliev et al. (2007) and introduce randomization of the structures along the LOS over a $100\,\mathrm{Mpc}\,h^{-1}$ scale in two steps. First, each $100\,\mathrm{Mpc}\,h^{-1}$ chunk of the data cube is randomly shifted (assuming periodic boundary conditions) and rotated in a direction perpendicular to the LOS. The shift can be positive or negative in any direction [x and (or) y] by an integer value between 0 and 512. The rotation can be clockwise or anticlockwise by an $n\pi/2$ angle ($n = 0, 1, 2, 3$). Secondly, the final data cube is produced by assembling the first $100\,\mathrm{Mpc}\,h^{-1}$ part from the x data cube, second from the y data cube, third from the z data cube and then back to the x data cube and so on to a distance that spans the comoving radial distance between redshifts 6 and 12.

3.3 Optical depth

The Thomson optical depth τ at redshift z is

$$\tau = c\sigma_T \int_0^z n_e \frac{(1+z)^2}{H(z)} dz, \tag{11}$$

where $c = 2.998 \times 10^8\,\mathrm{m\,s^{-1}}$ is the speed of light, $\sigma_T = 6.65 \times 10^{-29}\,\mathrm{m^2}$ the Thomson scattering cross-section for electrons, n_e the density of free electrons and $H(z)$ the Hubble constant at redshift z.

In our simulations, we split the integral into two parts. The first part represents the mean Thomson optical depth ($\bar{\tau}_{06}$) between redshifts 0 and 6 and the second, τ_{6z}, from redshift 6 to a desired redshift z. This choice is driven by the limited redshift range ($z \sim$ 6–11.5) of imminent radio astronomical projects designed to map the EoR. Under the assumption that reionization is completed by redshift 6, the mean Thomson optical depth $\bar{\tau}_{06}$ is 0.0517. Note that our patchy simulations are set to have a mean Thomson optical depth of 0.087, as obtained from the CMB data ($\tau = 0.087 \pm 0.017$; Komatsu et al. 2009).

3.4 Creating the kSZ and EoR maps

For clarity, we summarize the steps we follow to create the kSZ and EoR maps for a given scenario of the reionization history.

(i) Using the output of BEARS, data cubes for the density, radial velocity, helium and hydrogen fractions are produced.

(ii) Data cubes are randomized over the $100\,\mathrm{Mpc}\,h^{-1}$ scale along the redshift direction.

(iii) Using equation (11) the Thomson optical depth, τ, is calculated to a redshift z.

(iv) Using the integrand of equation (4), data cubes with the kSZ signal are produced as a function of redshift.

(v) Integrating along each LOS through the kSZ data cube, the integrated kSZ map is obtained. Note that we assume that the reionization is complete by redshift 6, so the integral in equation (4) spans the range $z > 6$.

(vi) Finally, the brightness temperature fluctuations, δT_b, are calculated using equation (8).

As examples, Figs 1 and 2 show slices through the simulated redshift cube of the cosmological 21 cm signal (δT_b) and the kSZ effect (δT_{kSZ}) in the case of the 'Stars' and the 'QSOs' patchy reionization models. The angular size of the slices is ∼0.°6.

In the following sections, we will use the kSZ and EoR maps produced from five different models of reionization.

(i) Homogeneous: reionization history is homogeneous and the ionized fraction follows

$$x_e = \frac{1}{1 + e^{k(z - z_{reion})}}, \tag{12}$$

with z_{reion} being set to 8.5 and $k = 2$, 4 and 10 which tunes the 'rapidness' of the reionization process. The mean ionization fractions $x_e(z)$ for the three different values of k (homogeneous models: HRH1, HRH2 and HRH3) are shown in Fig. 3.

(ii) Patchy stars: reionization history is patchy, gradual and extended with stars as the sources of ionization.

(iii) Patchy QSOs: reionization history is patchy and relatively fast with QSOs as the ionizing sources.

Apart from the difference in the global shape of the reionization histories driven by 'Stars' and 'QSOs' (see Fig. 4), the average sizes of the ionization bubbles are also smaller in 'Stars' compared to those of 'QSOs'. For a detailed description and comparison of reionization histories due to 'Stars' and 'QSOs', see Thomas et al. (2009).

The kSZ anisotropies from patchy reionization are induced by both fluctuations of the density field δ and ionization fraction δ_{x_e} (see equation 4). Santos et al. (2003) found that kSZ anisotropies from δ_{x_e} fluctuations dominate over the δ modulated fluctuations (OV effect). In order to test this result with our simulations, we split the integral in equation (4) into three parts and produce three integrated kSZ maps (for the 'Stars' model, see Fig. 5). The first term '$1 + \delta$' represents the density-induced secondary anisotropies (OV effect). The 'δ_{x_e}' term represents the secondary anisotropies due to patchiness in the reionization and '$\delta\delta_{x_e}$' represents a higher order anisotropy.

The mean and rms of the '$1 + \delta$', 'δ_{x_e}' and '$\delta\delta_{x_e}$' components of the simulated kSZ maps are given in Table 1 for patchy reionization in the 'Stars' and 'QSOs' models. The rms value of the maps is used as a measure of the fluctuations. We confirm that the 'δ_{x_e}' fluctuations are indeed larger than density-induced anisotropies ('δ') for both patchy reionization models. However, the difference between the 'δ_{x_e}' and 'δ' fluctuations is much larger for the 'Stars' reionization history model than for the 'QSOs' model. Also note that the third-order anisotropy ('$\delta\delta_{x_e}$') is not negligible in both reionization scenarios. For completeness, we also give the contribution from the pure Doppler term ('1') in equation (4).

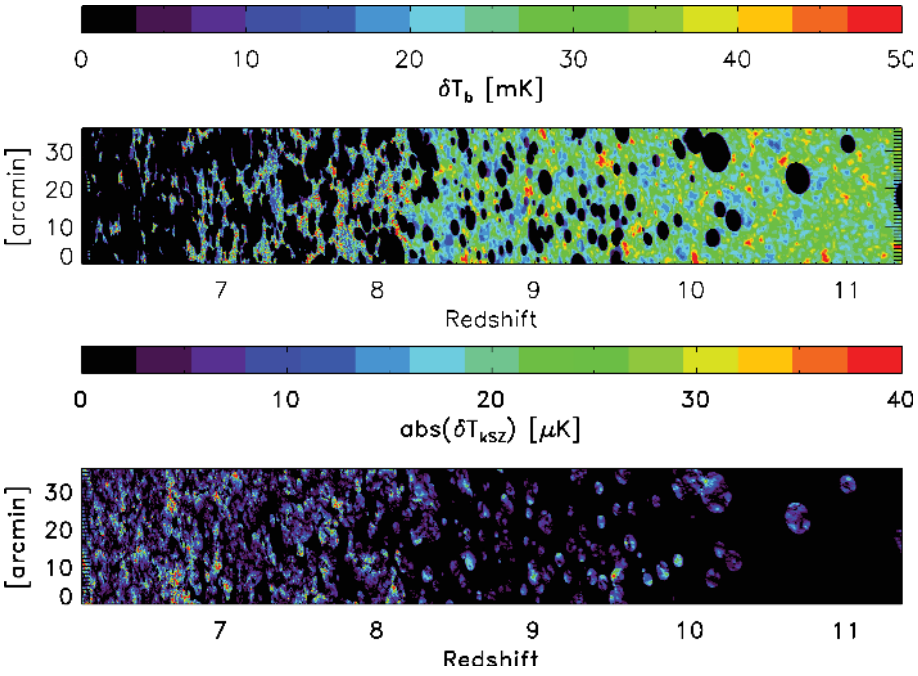

Figure 1. A slice through the simulated redshift cube of the cosmological 21 cm signal (top panel) and the kSZ effect (bottom panel) in the case of the 'Stars' patchy reionization model. The angular scale of the slices is ∼0.6.

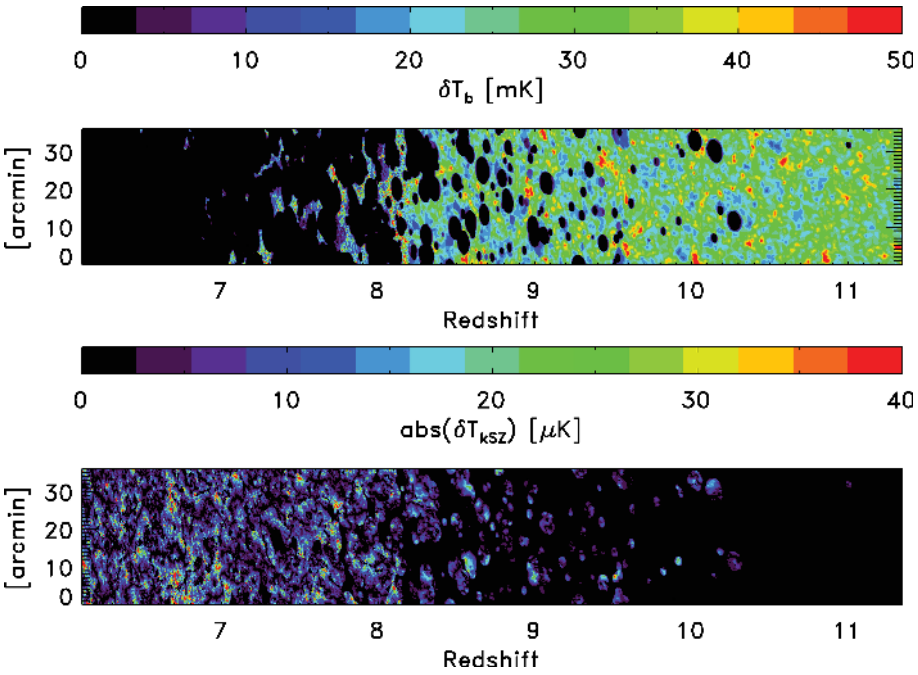

Figure 2. The same as Fig. 2 but for the 'QSOs' patchy reionization model.

4 CROSS-CORRELATION kSZ–EoR MAPS

The kSZ effect from the EoR is expected to be correlated with cosmological 21 cm maps for a homogeneous reionization history and anticorrelated when patchy (Cooray 2004; Salvaterra et al. 2005; Alvarez et al. 2006; Slosar et al. 2007; Adshead & Furlanetto 2008). In this section, the simulations described in Section 3 are used to explore the small angular scale cross-correlation between the kSZ effect and EoR maps for five different reionization histories. Further, we will fold in the influence of (i) the large-scale velocities on the kSZ effect and (ii) the pCMB fluctuations on the cross-correlation.

Throughout the paper, we will use a normalized cross-correlation in order to be able to compare results from different pairs of maps. The normalized cross-correlation between two images ($a_{i,j}$ and $b_{i,j}$) with the same total number of pixels n is defined at zero lag as

$$C_0 = \frac{1}{n-1} \sum_{i,j} \frac{(a_{i,j} - \bar{a})(b_{i,j} - \bar{b})}{\sigma_a \sigma_b}, \tag{13}$$

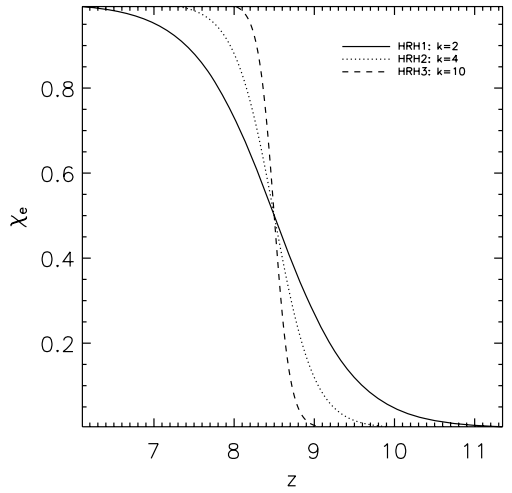

Figure 3. The ionization fraction x_e as a function of redshift for three different models of homogeneous reionization (HRH1, HRH2 and HRH3). All three models are defined by equation (12) but have different values of k (different reionization durations).

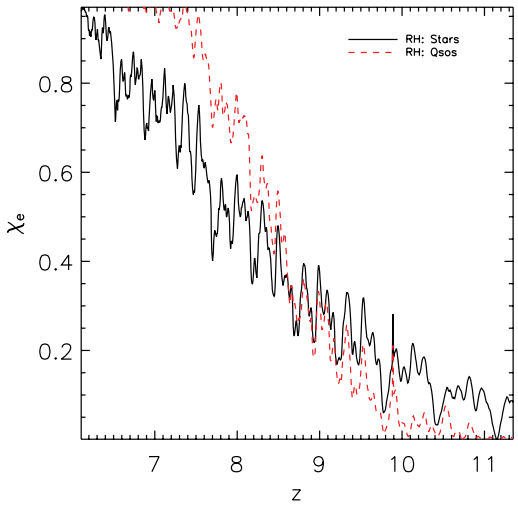

Figure 4. The mean ionization fraction x_e as a function of redshift for the 'Stars' and 'QSOs' patchy reionization models.

Table 1. The mean and rms of the '$1+\delta$', 'δ_{x_e}' and '$\delta\delta_{x_e}$' simulated kSZ maps for both the 'Stars' (see Fig. 5) and 'QSOs' patchy reionization models. C_0 is a cross-correlation coefficient at a zero lag between corresponding kSZ maps and the integrated EoR map (see Section 4). For completeness, we also list the results for the pure Doppler term ('1') in equation (4).

	$\delta T_{\rm kSZ}$	1	$1+\delta$	δ_{x_e}	$\delta\delta_{x_e}$	Total
Stars	mean (μK)	−0.004	0.03	0.58	0.02	0.63
	rms (μK)	0.14	0.80	1.74	0.40	2.00
	C_0	0.05	−0.003	−0.12	−0.06	−0.11
QSOs	mean (μK)	−0.002	0.03	0.27	0.01	0.30
	rms (μK)	0.15	0.93	1.28	0.28	1.57
	C_0	0.1	0.04	−0.08	−0.01	−0.06

where $\bar{a}(\bar{b})$ is the mean and $\sigma_a(\sigma_b)$ the standard deviation of image a (b). However, the cross-correlation between the kSZ and the EoR map needs to be considered more carefully, as we will explain in the following paragraph.

The fluctuations of the kSZ effect over the simulated map are both positive and negative, since the radial velocity v_r can be both positive and negative (see equation 4). In contrast, the EoR signal fluctuations in our simulations are always positive (see equation 8). When calculating the cross-correlation between these two maps, we are interested in finding the number of points at which both signals are present (homogeneous reionization model) or where one signal is present and the other absent (patchy reionization model). In other words, only the absolute value of the kSZ fluctuation is relevant in our calculation and not its sign.

4.1 Homogeneous reionization history

We explore the cross-correlation between the kSZ map and integrated EoR map in the case of three different homogeneous reionization histories (HRH1, HRH2 and HRH3). These histories are given by equation (12), with $k = 2$, 4 and 10 controlling the duration of reionization (see Fig. 3).

The cross-correlation between an integrated kSZ map and an integrated EoR map results in a coefficient $C_{0,\rm HRH1} = 0.10 \pm 0.03$ for an extended homogeneous reionization history (HRH1). For HRH2 $C_{0,\rm HRH2} = 0.21 \pm 0.02$ and for HRH3 $C_{0,\rm HRH3} = 0.24 \pm 0.02$. The errors are estimated by performing a Monte Carlo calculation with 200 independent realizations of the integrated kSZ and EoR maps using the randomization procedure explained in Section 3.

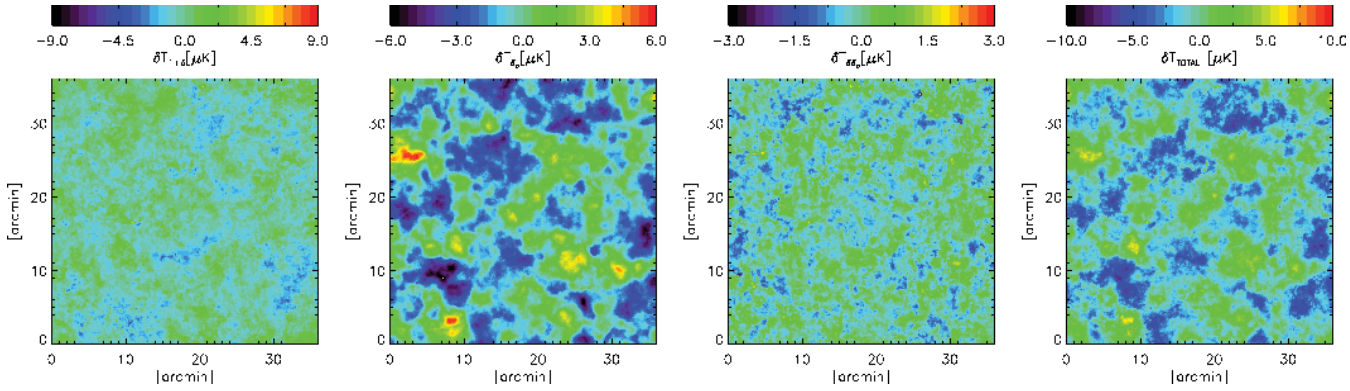

Figure 5. The simulated kSZ anisotropies induced by '$1+\delta$' (first panel), 'δ_{x_e}' (second panel) and '$\delta\delta_{x_e}$' (third panel) terms in equation (4) for the 'Stars' patchy reionization model. The kSZ anisotropies induced by all terms together in equation (4) are shown in the fourth panel ('TOTAL'). The mean and rms of the simulated kSZ maps are given in Table 1. Note that each map has its own colour scale.

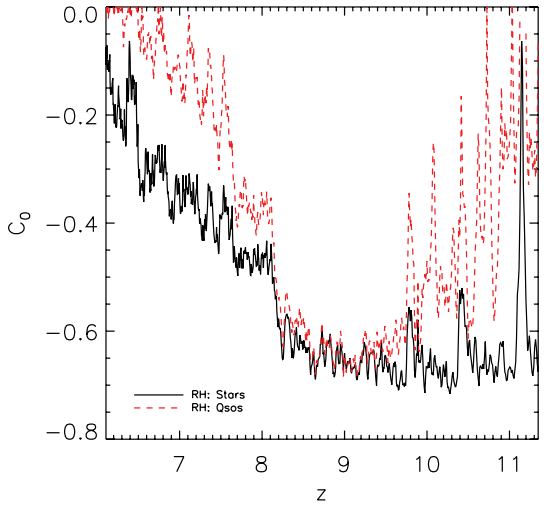

Figure 6. The zero-lag cross-correlation coefficient (C_0) between the kSZ map and the EoR map at a given redshift. The solid black line corresponds to the 'Stars' and the dashed red line to the 'QSOs' patchy reionization model. For both reionization models, we find an anticorrelation between the maps.

As expected, the integrated kSZ and EoR maps are correlated for homogeneous models of reionization. Furthermore, the correlation depends on the duration of reionization with larger values for more 'rapid' reionization. These results are in agreement with Alvarez et al. (2006).

4.2 Patchy reionization history

For the patchy reionization models, we first cross-correlate the kSZ and the EoR maps at a given redshift. The resulting zero-lag coefficient (C_0), as a function of redshift, is shown in Fig. 6. The solid black line represents the correlation for 'Stars' while the dashed red line the 'QSOs' patchy reionization model. As expected for patchy reionization in both models, the kSZ and the EoR maps anticorrelate at individual redshifts.

The anticorrelation obtained is also evident by visual inspection of the kSZ and EoR slices through the simulated redshift cubes (see Figs 1 and 2). One can see that the kSZ signal is present only at the regions where the EoR signal is not. This result is not surprising since the EoR signal is proportional to neutral hydrogen while the kSZ to the ionized, both of which are almost mutually exclusive.

In reality, we are not able to measure the kSZ effect at a certain redshift but only the integrated effect along the entire history. Thus, we can only cross-correlate the integrated kSZ map with the integrated EoR map and/or the EoR maps at different redshifts.[5]

Fig. 7 shows the integrated EoR and kSZ map for the 'Stars' (first two panels) and 'QSOs' (last two panels) patchy reionization models. The cross-correlation coefficients at zero lag for these two maps are $C_{0,\mathrm{Stars}} = -0.17$ and $C_{0,\mathrm{QSOs}} = -0.02$, respectively. In order to determine the error on the kSZ–EoR cross-correlation, we perform a Monte Carlo calculation. After creating 200 independent realizations of the integrated kSZ and EoR maps using the randomization procedure explained in Section 3, we calculate the cross-correlation coefficient for each pair of realizations. Finally, we calculate the mean and standard deviation of the cross-correlations.

[5]This is because, unlike the kSZ effect, we can potentially obtain redshift-specific information of neutral hydrogen via upcoming radio telescopes.

For the 'Stars' model we get $C_{0,\mathrm{Stars}} = -0.16 \pm 0.02$, while for the 'QSOs' model $C_{0,\mathrm{QSOs}} = -0.05 \pm 0.02$.

To understand the higher values of the cross-correlation coefficient in 'Stars' compared to the 'QSOs' model, one needs to analyse Fig. 4 and Table 1. It is evident from Fig. 4 that the reionization history is gradual and extended with stars as ionizing sources, compared to a shorter and sharper history with QSOs as ionizing sources. Moreover, the patchy term ('δ_{x_e}') of the kSZ fluctuations is much larger than the homogeneous component in the anisotropy ('δ') in the case of 'Stars' than for the 'QSOs' model (see Table 1). We showed earlier that the kSZ effect correlates with the cosmological 21 cm signal for homogeneous reionization and that the correlation is strongest for an 'instant' reionization history. We also obtain the same result by correlating different kSZ components with the integrated EoR map (see Table 1). Combining these results we see that the cross-correlation is driven by the patchy kSZ anisotropies in the 'Stars' model, while in the 'QSOs' model the homogeneous and patchy kSZ anisotropies tend to cancel each other. As a consequence, the anticorrelation in the 'QSOs' model is much weaker than that in 'Stars'.

In addition to the balance between homogeneous and patchy kSZ anisotropies that governs the (anti)correlation between the kSZ and the EoR maps, the size of the ionized bubbles also plays a key role. Recall that the average size of the ionization bubble is larger for 'QSOs'. As a result, the underlying structure within the ionized bubble will additionally reduce the anticorrelation and might change the scale of (anti)correlation.

From now on, we will concentrate on cross-correlations using 'Stars' since the 'QSOs' model does not show a significant anticorrelation. Fig. 8 shows the correlation coefficient as a function of lag ($C(\theta)$) between the integrated kSZ and the integrated EoR map. The dashed red lines represent the estimated error obtained from Monte Carlo simulations. As in Salvaterra et al. (2005), we find that the two signals are anticorrelated below a characteristic angular scale θ_c and this scale indicates the average size of the ionized bubbles which in our case is $\theta_c \approx 10$ arcmin.

Salvaterra et al. (2005) also showed that the amplitude of the anticorrelation signal increases with decreasing redshift and that the characteristic angular scale shows a redshift evolution. In order to test this in our simulation, we calculate the redshift evolution of the zero-lag cross-correlation coefficient between the integrated kSZ map and the EoR map at different redshifts (Fig. 9). To calculate the error in the cross-correlation, we generate 200 different realizations of the kSZ and corresponding EoR cubes using the randomization procedure explained in Section 3. Then, around a desired redshift we fix the kSZ effect to zero and integrate along the non-zero part of the kSZ cube. Finally, we cross-correlate the integrated kSZ map with the EoR map at the desired redshift and estimate the error on the cross-correlation between the integrated kSZ map and the EoR map at the certain redshift. Note that the EoR map at a certain redshift is produced by integrating a $100\,h^{-1}$ Mpc volume around that redshift.

From Fig. 9, we find no coherent redshift evolution of the anticorrelation signal and at a few redshifts the two signals actually correlate instead of anticorrelating. The correlation at a given redshift is caused by the following. (i) The patchy nature of the EoR signal, which implies that there are some redshifts at which the EoR map contains none or only a few small ionized bubbles. If one correlates such an EoR map with the integrated kSZ map, the outcome is a correlation between the two, and because of an insignificant number of the ionization bubbles there is no contribution to the anticorrelation (ii) The patchy nature of the kSZ signal. There are

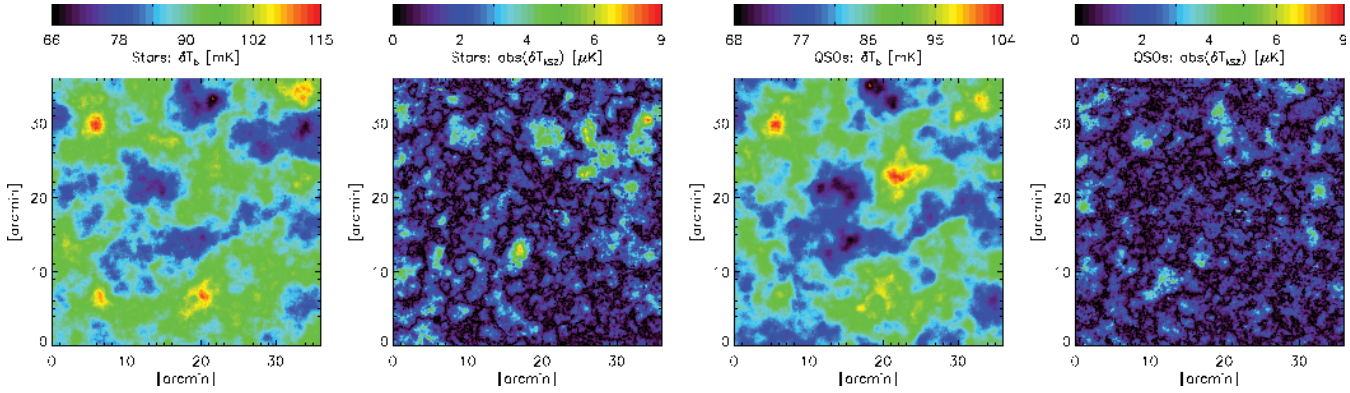

Figure 7. The integrated EoR and kSZ map for the 'Stars' (first two panels) and 'QSOs' (second two panels) patchy reionization models. The mean cross-correlation coefficient at the zero lag between the integrated EoR map and integrated kSZ map is $C_{0,\mathrm{Stars}} = -0.16 \pm 0.02$ for the 'Stars' and $C_{0,\mathrm{QSOs}} = -0.05 \pm 0.02$ for the 'QSOs' model.

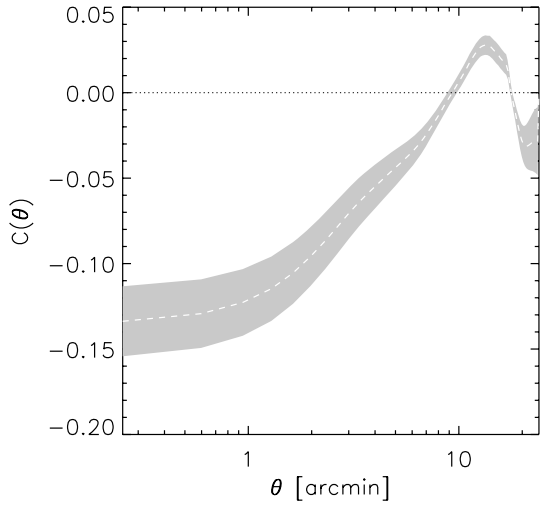

Figure 8. The cross-correlation between the integrated EoR map and integrated kSZ map as a function of lag ($C(\theta)$) for the 'Stars' reionization history scenario (dashed white line). The grey-shaded surface represents the estimated error obtained by the Monte Carlo simulation. Note that the correlation coefficient at the zero lag is $C_0 = -0.16 \pm 0.02$.

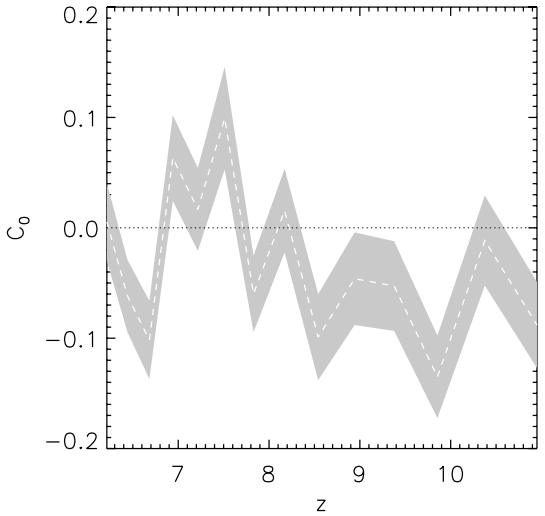

Figure 9. The redshift evolution of the zero-lag correlation coefficient between the integrated kSZ map and the EoR map at the certain redshift. The result is shown for the 'Stars' reionization history model. Note that the EoR map at a certain redshift is produced by integrating $100\,h^{-1}$ Mpc volume around that redshift.

some redshifts where the kSZ signal from a certain ionization bubble does hardly or not at all contribute to the integrated kSZ map. This could happen due to a weak kSZ signal from a certain ionized bubble or due to cancellation of the kSZ signal from another ionization bubble along the LOS.

To illustrate the patchy nature of the kSZ signal and its implications to the cross-correlation, we plot the kSZ signal, $\delta T_{\mathrm{kSZ}}(z)$, and its cumulative integral, $\int_{z_{\mathrm{max}}}^{z} \delta T_{\mathrm{kSZ}}(z)\mathrm{d}z$, as a function of redshift, for two random LOSs (see Fig. 10). Note from the bottom panel of Fig. 10 that the kSZ signal, as its progress towards the lower redshifts, fluctuates randomly between positive and negative values. Thus, there is no coherent contribution (continuous increase or decrease) to the kSZ signal over the whole redshift range. See also figs 12 and 13 in Iliev et al. (2007) who reached a similar conclusion.

We repeat the analysis of the redshift evolution of the zero-lag cross-correlation coefficient for different bin sizes along redshift (e.g. redshift bins corresponding to $20\,h^{-1}$ Mpc in comoving coordinates). However, the result does not differ significantly. We also calculate the redshift evolution of the characteristic angular scale (θ_{c}), but we do not find any coherent evolution. This result is driven by the fact that the contribution of the kSZ signal from a certain redshift to the integrated kSZ map is not significant or even non-existent. As a result, if there is no coherent contribution (continuous increase or decrease) to the integrated kSZ map over the whole redshift range there will be no coherent redshift evolution of the kSZ–EoR cross-correlation signal (Fig. 10).

The discrepancy between our results and those of Salvaterra et al. (2005) is due to (i) the difference in the method to calculate the cross-correlation coefficient and (ii) the different sizes of the computational boxes.

Salvaterra et al. first calculated the cross-correlation coefficient (not normalized with the rms) between a certain kSZ and EoR map. Then, they scrambled both maps without keeping any structural information and calculated the cross-correlation coefficient. They compared the coefficients in the two cases to draw their conclusion. In contrast to Salvaterra et al., we first calculate the normalized cross-correlation coefficient (see equation 13) between a pair of kSZ–EoR maps. And then for comparison, we perform a Monte Carlo simulation to generate different realizations of the kSZ and the EoR maps. However, despite the cross-correlation procedure

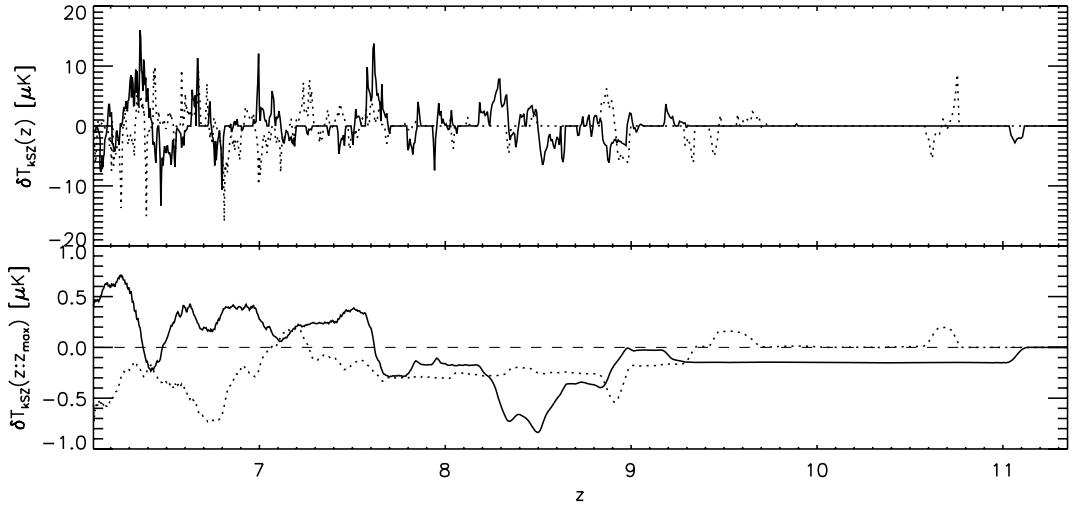

Figure 10. Top panel: two random (solid and dotted) LOs through the 'Stars' kSZ cube, $\delta T_{\rm kSZ}(z)$, averaged over 10 pixels (∼0.7 arcmin) at each redshift. Bottom panel: for the same LOSs the cumulative integral of the kSZ effect, $\int_{z_{\rm max}}^{z} \delta T_{\rm kSZ}(z){\rm d}z$. Note that there is no coherent contribution (continuous increase or decrease) of the cumulative kSZ effect over the whole redshift range.

used, once the pCMB fluctuations are included we are not able to find any significant kSZ–EoR cross-correlation (see Section 4.4).

In addition, Salvaterra et al. used fairly small computational boxes (4 and 20 h^{-1} Mpc) compared to our 100 h^{-1} Mpc box. Since most of the signal comes around the mid-point of reionization, the velocity field and the typical size of reionization bubbles at that redshift put a strong constraint on the size of simulation that one can use. In fig. 2 of Salvaterra et al. (2005), one can see that at 50 per cent reionization, the size of the reionization bubble is about half the simulation box. This means that no matter how one randomizes the box, the bubble will still overlap with the position of the bubble in the next or previous snapshot. Moreover, the small 20 h^{-1} Mpc simulation box misses ∼90 per cent of the velocity power as given by the linear theory (see section 4.3 in Iliev et al. 2007), and this could lead to velocity coherence. In other words, the redshift 'enhancement' of the kSZ signal is not fully removed.

4.3 Large-scale velocity

Our simulation volume is (100 h^{-1} Mpc)^3 (see Section 3). Thus, large-scale velocities associated with bulk motions, on scales of $\gtrsim$100 h^{-1} Mpc, are missing. The missing velocities represent ∼50 per cent of the total power in the velocity field as given by the linear theory.

Iliev et al. (2007) showed that the large-scale velocities on scales of $\gtrsim$100 h^{-1} Mpc increase the kSZ signal. Motivated by this result, we approximately account for the missing large-scale velocities in a similar way as Iliev et al. (2007): first, we assume that every 100 h^{-1} Mpc chunk of our simulation cube has a random large-scale velocity component $v_{\rm LS}$. Since our simulation cube is produced using 15 simulation boxes (100 h^{-1} Mpc), we need in total 15 $v_{\rm LS}$. We randomly choose a realization of the 15 $v_{\rm LS}$ based on a velocity field power spectrum from linear theory. By doing this, we ensure that the velocities are correlated at large scales. Finally, we add the missing $v_{\rm LS}$ component to each 100 h^{-1} Mpc chunk of the simulated cube.

Based on 200 realizations of the large-scale velocity field, we have found that the large-scale velocities increase the kSZ signal during the EoR by 10 per cent. But on average we do not find any significant increase or decrease in the kSZ–EoR cross-correlation. However, for ∼20 per cent of all large-scale velocity realizations we find an increase in the cross-correlation signal by a factor of 2 or larger and for ∼2 per cent a factor of 3 or larger.

4.4 Primary CMB

Up to now, our cross-correlation analysis only took into account the secondary CMB anisotropies generated by the kSZ effect. In the actual experiment, the CMB data will comprise not only the kSZ anisotropies which are secondary, but also the primary and other secondary CMB anisotropies (for a recent review, see Aghanim et al. 2008). In this subsection, we will examine the influence of the pCMB fluctuations on the detectability of the kSZ–EoR cross-correlation.

We simulate the pCMB fluctuations in the following way: first the CMB power spectra are obtained using CMBFAST (developed by U. Seljak and M. Zaldarriaga in 2003) and then the map of the primary anisotropy is produced as a random Gaussian field with this power spectrum. An example of the simulated pCMB map is shown in Fig. 11. The size of the map corresponds to the size of the simulated EoR and kSZ maps. Note the lack of power at small scales due to the Silk damping (Silk 1967).

In order to calculate the noise in the cross-correlation introduced by the pCMB fluctuations, we generate 200 different realizations of the pCMB fluctuations. We then add secondary kSZ anisotropies induced by the 'Stars' (map shown in Fig. 7) and calculate the cross-correlation between the pCMB+kSZ map and the integrated cosmological 21 cm map. The zero-lag cross-correlation coefficient obtained is 0.0 ± 0.3. The noise introduced by the pCMB fluctuations is thus too large to detect any significant kSZ–EoR (anti)correlation. However, one has to remember that the pCMB anisotropies are damped on small angular scales and that on these scales the secondary anisotropies are the dominant component of the CMB power spectra (see Fig. 12).[6] Utilizing this fact, one can

[6]Note that a harmonic multipole l translates to degrees as $\theta[^\circ] = 180^\circ/l$. The angular resolution of the simulated maps is ∼5 arcsec, which translates to $l_{\rm max} \sim 1.3 \times 10^5$. The maps are expected to convey the physical information for $1.5 \times 10^3 \lesssim l \lesssim 1.3 \times 10^5$.

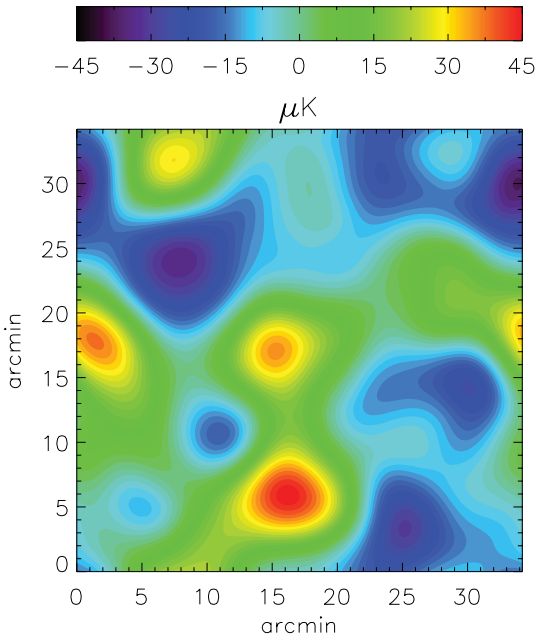

Figure 11. The map of the pCMB fluctuations generated as a Gaussian random field with the power spectrum obtained from the CMBFAST algorithm.

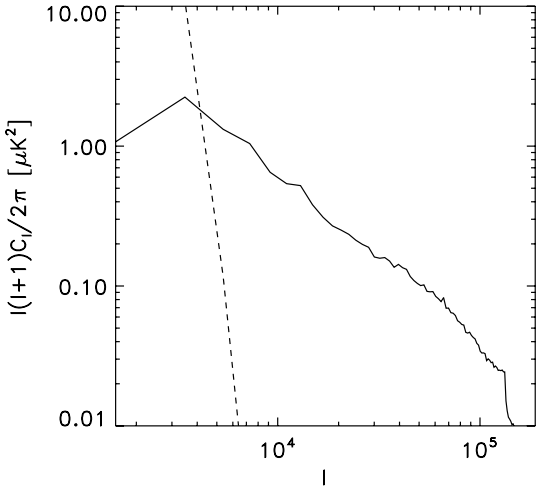

Figure 12. The power spectra of pCMB fluctuations (dotted line) and kSZ anisotropies obtained from the simulated maps (solid line).

do a cross power spectrum and see the correlation as a function of the angular scale. Pursuing this lead, we first calculate the kSZ–EoR cross spectrum without and then with the pCMB added to the kSZ map.

The cross spectrum (C_l^X) between the two images of a small angular size is given by

$$C_l^{\rm X} \simeq P_k^{\rm X} = \frac{1}{n_k} \sum_{p,q \in k} A_{p,q} \cdot B_{p,q}^*, \qquad (14)$$

where $A_{p,q}$ is the Fourier transform of the first image, $B_{p,q}^*$ the complex conjugate of the Fourier transform of the second image and n_k the number of points in the kth bin ($k = \sqrt{p^2 + q^2}$). Note that we assume the 'flat-sky' approximation (e.g. White et al. 1999): $k^2 P(k) \simeq \frac{l(l+1)}{(2\pi)^2} C_l \mid_{l=2\pi k}$ which is valid for $l \gtrsim 60$.

Fig. 13 shows the cross power spectrum between the kSZ anisotropies and the integrated cosmological 21 cm map for reionization due to 'Stars'. It is evident from the plot that the two images anticorrelate on large scales ($l \lesssim 8000$), but that the anticorrelation becomes weaker towards smaller angular scales. At angular scales $l \gtrsim 8000$, there is no (anti)correlation.

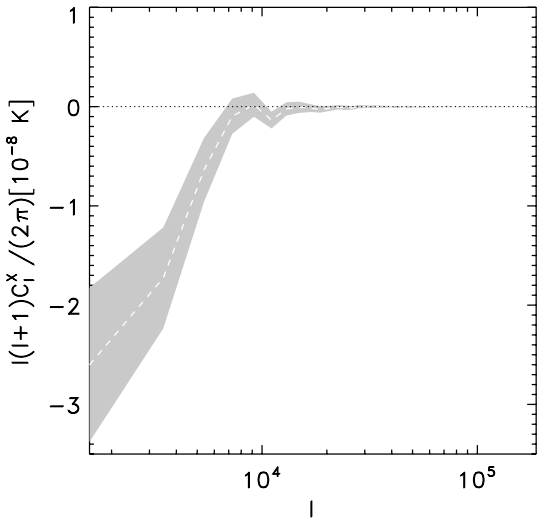

Figure 13. The cross spectrum (see equation 14) between the integrated kSZ map and integrated EoR map for the 'Stars' reionization history (dashed white line). The grey-shaded surface represents the estimated error obtained by the Monte Carlo simulation. Note that the pCMB fluctuations are not included.

We also calculate the cross power spectrum between the integrated EoR map and integrated kSZ map with pCMB fluctuations included. In this case, the noise introduced by the pCMB is too large to find any significant correlation at scales $l \lesssim 8000$.

This result might be driven by the simulation box size and reionization scenarios considered in this study and does not mean that a cross-correlation signal is absent at all scales and reionization histories. In order to test this, one needs to explore the kSZ–EoR cross-correlation using simulations with box sizes larger than $100\,h^{-1}$ Mpc.

4.5 Additional cross-correlation techniques

For better understanding of the properties of the kSZ–EoR cross-correlation, and with the hope of being able to find the cross-correlation signal in the presence of the pCMB fluctuation, in this subsection we apply techniques of filtering, wavelet decomposition and relative entropy to our data. We will only use the integrated kSZ map and integrated EoR map from the 'Stars' model of reionization, since as we saw above, this model produces the strongest cross-correlation signal. Note that in the following analysis, we first use the kSZ and the EoR maps and then as a second step include the pCMB fluctuations.

Fig. 14 shows the zero-lag cross-correlation coefficient for the three different filtering procedures. The first one uses a high-pass, the second a low-pass and the third a band-pass filter that passes out only a certain scale. In all three cases, the filter is based on the 'Top hat' function. We filter out the desired scale from both the kSZ map and the EoR map and calculate the cross-correlation coefficient at zero lag. The results are shown for the low-pass and high-pass filters as a function of the FWHM of the filter and for the band-pass filter as a function of scale.

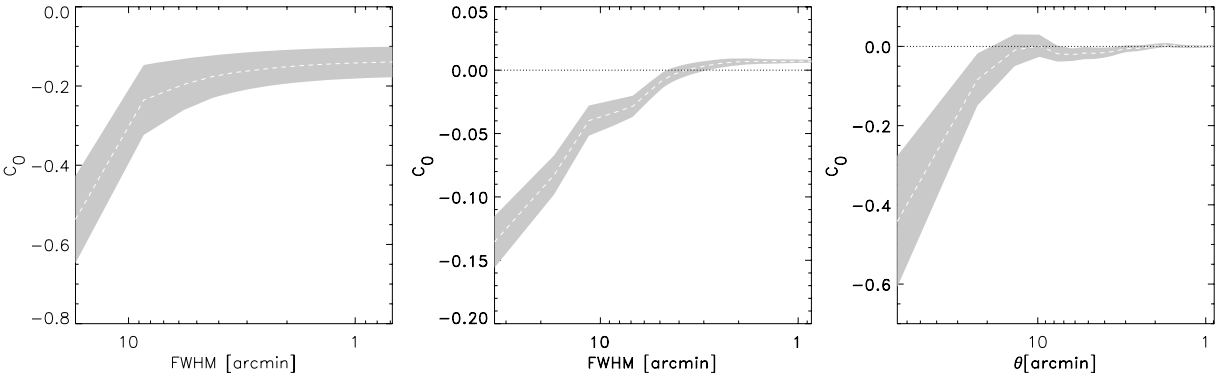

Figure 14. The zero-lag cross-correlation coefficient as a function of the three different filtering procedures. The first one uses a high-pass filter, the second one uses a low-pass filter and the third a band-pass filter that passes only a certain scale. In all three cases, the filter is based on the 'Top hat' function. The dashed white line is the mean and the grey-shaded surface represents the estimated error obtained by the Monte Carlo simulation.

The plot on the left-hand panel in Fig. 14 implies that the anticorrelation is strongest on the largest scales of the map. By adding smaller scales, the correlation coefficient decreases meaning that smaller scales introduce noise in the correlation. The middle panel in Fig. 14 suggests the same behaviour. By removing the large scales, the cross-correlation signal becomes very weak. Finally, the third panel of Fig. 14 suggests that the large scales are indeed the dominant component of the anticorrelation signal.

As a next step in our analysis, we include the pCMB fluctuations. However, we obtain the same result as discussed in Section 4.4. On the scales where the kSZ anisotropies dominate over the primary anisotropies, either the anticorrelation signal is too weak or the noise introduced by residuals of the pCMB fluctuations is too large to find any statistically significant kSZ–EoR (anti)correlation.

The wavelet analysis of the maps is preformed using Daubechies and Coiflet wavelet functions. Both the integrated kSZ map with added pCMB fluctuations and the integrated EoR map are decomposed to a certain wavelet mode and then they are cross-correlated. Because the outcome is similar to that of filtering, we will not discuss this further.

The last method applied to the data is the 'relative entropy', also known as the Kullback–Leibler distance. The relative entropy is a measure of the information shared between two variables (two images) by comparing the normalized distribution of the two. This method also did not produce any significant result.

5 SUMMARY AND CONCLUSIONS

This paper presents a cross-correlation study between the kSZ effect and cosmological 21 cm signal produced during the EoR. The study uses an N-body/SPH simulation along with a 1D radiative transfer code (the BEARS algorithm; Thomas et al. 2009) to simulate the EoR and to obtain maps of the cosmological 21 cm signal and the kSZ effect. The maps are produced using a $100\,h^{-1}$ Mpc comoving simulation box for five different (three homogeneous and two patchy) models of reionization history. The homogeneous model with varying degrees of 'rapidness' of the reionization process is given by equation (12). The patchy reionization histories include one by 'Stars' (gradual) and the other by 'QSOs' (instant).

For a homogeneous reionization history, we find that the kSZ map and the integrated EoR map are correlated and that the correlation depends on the duration of reionization with larger values for more 'rapid' models. This result agrees with the analytical kSZ–EoR cross-correlation analysis carried out by Alvarez et al. (2006).

For patchy reionization models, we find that the kSZ temperature fluctuations are of a few μK level (see Table 1) and are in agreement with previous results (Salvaterra et al. 2005; Iliev et al. 2007). In addition, we show that the temperature fluctuations induced by the patchiness of the reionization process ('δ_{x_e}' term in equation 4) are larger than the density-induced fluctuations (homogeneous '$1+\delta$' term in equation 4). The difference between the two is stronger for the extended history ('Stars' model) than for the more rapid reionization history ('QSOs' model) (see Table 1).

As a first step in the kSZ–EoR cross-correlation study of patchy reionization histories, we cross-correlate the kSZ map and EoR map at each redshift (see Figs 1 and 2). As expected, the kSZ and the EoR map anticorrelate at certain redshifts (see Fig. 6).

We then cross-correlate the integrated cosmological 21 cm map and the integrated kSZ map for patchy reionization (see Fig. 7). The two signals show significant anticorrelation only in the 'Stars' model ($C_{0,\mathrm{Stars}} = -0.16 \pm 0.02, C_{0,\mathrm{QSOs}} = -0.05 \pm 0.02$.). The result is driven by the balance between homogeneous and patchy ('$1+\delta$' and 'δ_{x_e}' terms in equation 4) kSZ anisotropies and the average size of the ionized bubbles. Since the homogeneous kSZ anisotropies correlate and patchy kSZ anisotropies anticorrelate with the cosmological 21 cm maps, the two effects tend to cancel each other. In addition, the average size of the ionization bubble is larger for 'QSOs' than for the 'Stars' model and the structure of matter within the ionized bubble reduces the cross-correlation. As a consequence, the kSZ–EoR anticorrelation is much stronger for the extended ('Stars' model) reionization history than for a more instant history ('QSOs' model).

For a patchy model of reionization, we estimate the redshift evolution of the correlation coefficient (C_0) and characteristic angular scale θ_{C}. This was done by cross-correlating the integrated kSZ maps with the EoR maps at different redshifts (see Fig. 9). In contrast to Salvaterra et al. (2005), we do not find any significant coherent redshift evolution of C_0 and θ_{C}. This discrepancy is caused by the difference in the procedure used for calculating cross-correlation and the different size of the computational boxes.

The influence of the missing large-scale velocities on the kSZ signal and kSZ–EoR cross-correlation was investigated. Although the large-scale velocities increase the kSZ signal by 10 per cent, we do not find, on average, any significant change in the kSZ–EoR cross-correlation. However, for ∼20 per cent of large-scale velocity realizations we find an increase in the cross-correlation signal by

a factor of 2 or larger and for ∼2 per cent by a factor of 3 or larger.

The data from CMB experiments contain both the secondary (e.g. kSZ) and primary anisotropies. We calculate the noise in the kSZ–EoR cross-correlation introduced by the pCMB fluctuations and found that its addition reduces the cross-correlation signal to zero ($C_0 = 0.0 \pm 0.3$). The cross-correlation was also performed on scales where the kSZ anisotropies dominate over the pCMB fluctuations ($l \gtrsim 4000$; see Fig. 12). We have done this by calculating cross-power spectra (Fig. 13), applying different filtering methods (Fig. 14) on the data and by doing wavelet decomposition. However, the outcome of the analysis is that on the scales where the kSZ anisotropies dominate over primary, either the anticorrelation signal is too weak or the noise introduced by residuals of the pCMB fluctuations is still too large to find any statistically significant kSZ–EoR (anti)correlation.

As a further check, we calculate the kSZ–EoR cross-correlation using the simulation from Iliev et al. (2007) ('f250C' $100\,h^{-1}$ Mpc simulation). The reionization history of this model is similar to our 'QSOs' model. The reionization history is relatively sharp and instant. The cross-correlation coefficient at zero lag for the integrated kSZ map and integrated EoR map is $C_0 = -0.04 \pm 0.02$. The result is in agreement with the result obtained from the 'QSOs' model. We also calculated the redshift evolution of the zero-lag cross-correlation coefficient and have found no coherent redshift evolution.

In view of all the results obtained from our kSZ–EoR cross-correlation study, we conclude that the kSZ–EoR anticorrelation on scales captured by our simulation box (∼0.°6) is not a reliable technique for probing the EoR. However, there is still hope that we will be able to find the correlation between the kSZ and EoR signals on scales larger than ∼1°, where the patchiness of the ionization bubbles should average out (Alvarez et al. 2006; Tashiro et al. 2009). Finally, it is important to note that the kSZ signal induced during the EoR could still be detected in the power spectra of the CMB and used to place some additional constraints on this epoch in the history of our Universe.

ACKNOWLEDGMENTS

We acknowledge discussion with the LOFAR-EoR key project members. We thank I. Iliev for providing us with the Iliev et al. (2007) ('f250C' $100\,h^{-1}$ Mpc) simulation, J. Schaye and A. Pawlik for their dark matter simulation and A. Ferrara for useful comments. We are also thankful to the anonymous referee for his illustrative and constructive comments. As LOFAR members VJ, SZ, LVEK and RMT are partly funded by the European Union, European Regional Development Fund and by 'Samenwerkingsverband Noord-Nederland', EZ/KOMPAS.

REFERENCES

Adshead P. J., Furlanetto S. R., 2008, MNRAS, 384, 291
Aghanim N., Majumdar S., Silk J., 2008, Rep. Progress Phys., 71, 066902
Alvarez M. A., Komatsu E., Doré O., Shapiro P. R., 2006, ApJ, 647, 840
Ciardi B., Madau P., 2003, ApJ, 596, 1
Cooray A., 2004, Phys. Rev. D, 70, 063509
Doré O., Holder G., Alvarez M., Iliev I. T., Mellema G., Pen U.-L., Shapiro P. R., 2007, Phys. Rev. D, 76, 043002
Dvorkin C., Hu W., Smith K. M., 2009, Phys. Rev. D, 79, 107302
Fan X. et al., 2006, AJ, 132, 117
Field G., 1958, Proc. IRE, 132, 240
Field G. B., 1959, ApJ, 129, 536
Furlanetto S. R., Zaldarriaga M., Hernquist L., 2004, ApJ, 613, 16
Gnedin N. Y., Jaffe A. H., 2001, ApJ, 551, 3
Gunn J. E., Peterson B. A., 1965, ApJ, 142, 1633
Harker G. et al., 2009a, MNRAS, 397, 1138
Harker G. J. A. et al., 2009b, MNRAS, 393, 1449
Iliev I. T., Pen U.-L., Bond J. R., Mellema G., Shapiro P. R., 2007, ApJ, 660, 933
Jelić V. et al., 2008, MNRAS, 389, 1319
Komatsu E. et al., 2009, ApJS, 180, 330
Labropoulos P. et al., 2009, arXiv:0901.3359
Lee K.-G., 2009, ApJ, submitted (arXiv:0902.1530)
Madau P., Meiksin A., Rees M. J., 1997, ApJ, 475, 429
Ostriker J. P., Vishniac E. T., 1986, ApJ, 306, L51
Page L. et al., 2007, ApJS, 170, 335
Salvaterra R., Ciardi B., Ferrara A., Baccigalupi C., 2005, MNRAS, 360, 1063
Santos M. G., Cooray A., Haiman Z., Knox L., Ma C.-P., 2003, ApJ, 598, 756
Silk J., 1967, Nat, 215, 1155
Slosar A., Cooray A., Silk J. I., 2007, MNRAS, 377, 168
Spergel D. N. et al., 2007, ApJS, 170, 377
Sunyaev R. A., Zeldovich Y. B., 1970, Ap&SS, 7, 3
Tashiro H., Aghanim N., Langer M., Douspis M., Zaroubi S., 2008, MNRAS, 389, 469
Tashiro H., Aghanim N., Langer M., Douspis M., Zaroubi S., Jelic V., 2009, MNRAS, submitted (arXiv:0908.1632)
Thomas R. M., Zaroubi S., 2008, MNRAS, 384, 1080
Thomas R. M. et al., 2009, MNRAS, 393, 32
Vishniac E. T., 1987, ApJ, 322, 597
White M., Carlstrom J. E., Dragovan M., Holzapfel W. L., 1999, ApJ, 514, 12
Wouthuysen S. A., 1952, AJ, 57, 31
Zahn O., Zaldarriaga M., Hernquist L., McQuinn M., 2005, ApJ, 630, 657
Zaroubi S., Thomas R. M., Sugiyama N., Silk J., 2007, MNRAS, 375, 1269
Zeldovich Y. B., Sunyaev R. A., 1969, Ap&SS, 4, 301
Zhang P., Pen U.-L., Trac H., 2004, MNRAS, 347, 1224

This paper has been typeset from a TEX/LATEX file prepared by the author.